Journal of Geophysical Research: Solid Earth

RESEARCH ARTICLE
10.1029/2018JB015523

The Gravitational Stability of Lenses in Magma Mushes: Confined Rayleigh-Taylor Instabilities

G. Seropian[1,2], A. C. Rust[1], and R. S. J. Sparks[1]

[1]School of Earth Sciences, University of Bristol, Bristol, UK, [2]Now at Department of Geological Sciences, University of Canterbury, Christchurch, New Zealand

Key Points:
- Melt-mush Rayleigh-Taylor instabilities are generally laterally confined, which reduces the growth rate
- The confined instability growth rate only depends on the mush viscosity, melt lens diameter, and density difference
- Mush rheology is a key control on size and frequency of eruptions related to buoyancy instabilities

Correspondence to:
G. Seropian,
gs16066@my.bristol.ac.uk

Citation:
Seropian, G., Rust, A. C., & Sparks, R. S. J. (2018). The gravitational stability of lenses in magma mushes: Confined Rayleigh-Taylor instabilities. *Journal of Geophysical Research: Solid Earth*, *123*, 3593–3607. https://doi.org/10.1029/2018JB015523

Received 22 JAN 2018
Accepted 14 APR 2018
Accepted article online 30 APR 2018
Published online 2 MAY 2018

Abstract In the current paradigm, magma primarily exists in the crust as a crystalline mush containing distributed melt lenses. If a melt-rich (or fluid) lens is less dense than the overlying mush, then Rayleigh-Taylor (RT) instabilities will develop and could evolve into spheroids of ascending melt. Due to contrasting melt-mush rheologies, the theoretical RT instability wavelength can be orders of magnitude larger than the magmatic system. We explored how this confinement affects the gravitational stability of melt lenses through laboratory experiments with pairs of liquids with one layer much thinner and up to $2.2 \cdot 10^5$ times less viscous than the other; we extended the viscosity ratio to 10^6 with linear stability analysis. We found the growth rate of a bounded RT instability is approximately $\frac{\Delta\rho g D}{6\pi\mu_2}$, where $\Delta\rho$ is the difference in density between the fluids, g is gravity, D is the container diameter, and μ_2 is the viscosity of the thicker viscous layer. This differs from the unbounded case, where the growth rate also depends on the thickness and viscosity of the thin, low-viscosity layer. Applying the results to melt lenses in magmatic mushes, we find that for the ranges of expected rheologies, the timescales for development of the instability, and the volumes of packets of rising melt generated span very wide ranges. They are comparable with the frequencies and sizes of volcanic eruptions and episodes of unrest and so suggest that RT instabilities in mush systems can cause episodic volcanism.

1. Introduction

A major challenge of modern volcanology concerns subsurface magma transport and accumulation. Conceptual models are emerging that depict subsurface systems as large uneruptible crystalline networks (mushes) containing heterogeneously distributed pockets of eruptible magma and exsolved volatiles that can extend deep in the crust and down to the mantle (e.g., Bachmann & Huber, 2016; Cashman et al., 2017). The dynamics of igneous mush systems has become a dominant theme in contemporary magma physics (e.g., Bergantz et al., 2017; Dufek & Bachmann, 2010; Parmigiani et al., 2014) and a key feature of interpretations of geophysical, geochemical, and petrological data (e.g., Jaxybulatov et al., 2014; Putirka, 2017).

One aspect of igneous mush dynamics is the development of buoyancy instabilities related to intrusion of new magma or segregation of melt- or fluid-rich layers within a mush, leading to magma or fluid ascent through the mush. Magmas, melts, and fluids are commonly less dense than the overlying mush; therefore, Rayleigh-Taylor (RT) instabilities develop naturally wherever buoyant layers form. However, for some conditions (e.g., sufficiently high mush viscosity) the growth rate may be sufficiently slow that other processes (e.g., solidification due to cooling) dominate.

The viscosity contrast between a buoyant layer and an igneous mush is typically very large. For example, if we consider mushes with effective viscosities from 10^{13} Pa·s for melt-rich mush (~40% melt) to 10^{17} Pa·s for melt-poor mush (<10% melt, Costa et al., 2009; Lejeune & Richet, 1995), and melt (magma) lenses with viscosities of $1 - 10^5$ Pa·s (basalt to wet rhyolite), then the viscosity ratios are of order $10^8 - 10^{17}$. There is a theory for RT instabilities for infinite horizontal layers with very high viscosity ratios (Whitehead & Luther, 1975), which has been verified in experiments with viscosity ratios of up to a few hundred. Although never tested experimentally, this theory should be applicable to the much higher viscosity ratios expected in lens-mush magmatic systems. However, a consequence of the high viscosity ratios is that the horizontal dimension of a magma reservoir is commonly much less than the theoretical fastest-growing wavelength assuming an infinite horizontal layer (Figure 1). Thus, it is necessary to consider cases in which the buoyant layer is confined by boundaries separated by lengths much less than the optimum wavelength. The purpose of this study

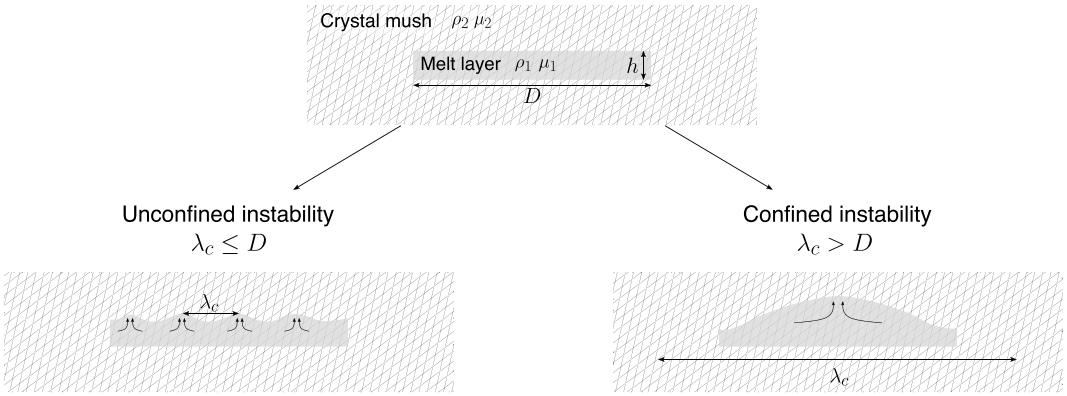

Figure 1. Sketch of an eruptible melt-rich layer within a much more viscous crystal mush. Rayleigh-Taylor instabilities arise due to density difference; however, the theoretical wavelength of instability λ_c may be much larger than the melt layer diameter D.

is to address this issue through experimental and theoretical approaches and then to apply the results to understanding RT instabilities in igneous mushes. The suggestion that RT instabilities can control the frequency of volcanic eruptions is explored.

2. Mush-Melt RT Instabilities

2.1. RT Instabilities

A RT instability occurs when a dense fluid overlies a less dense fluid. Such instabilities can arise in magmatic systems when a layer of buoyant melt is trapped within a denser crystalline mush. The full dynamics of RT instability are too complex to be described analytically. Nonetheless, linear stability analysis (LSA) provides good insight into the early stage, during which small initial perturbations of the interface grow exponentially (Waddell et al., 2001).

Mush-melt RT instabilities involve very high viscosity ratios. The relevant low Reynolds number RT instability formalism for such high viscosity contrasts was developed by Whitehead and Luther (1975). They analyzed the case of a thin layer of light Newtonian fluid (density ρ_1, viscosity μ_1) below a deep layer of denser Newtonian fluid (ρ_2, μ_2); both fluids are horizontally infinite (Figure 1). In this scenario, for a free slip boundary condition (BC) below the thin layer, and a large viscosity ratio ($\varepsilon = \frac{\mu_2}{\mu_1} \gg 1$), there exists a fastest-growing mode, the critical mode, with wavelength λ_c and growth rate n_c given by

$$\lambda_c = \frac{4\pi}{2.88} h \varepsilon^{1/3}, \tag{1}$$

$$n_c = 0.232 \frac{g \Delta \rho h}{\mu_2} \varepsilon^{1/3}, \tag{2}$$

where h is the thickness of the thin layer and $\Delta\rho = |\rho_2 - \rho_1|$ is the density difference. It is also assumed that the wave-like perturbations are small, with amplitude less than $\sim 0.4\lambda_c$. These equations have been modified to investigate the thickening of a buoyant layer at a fixed rate (i.e., constant $\frac{dh}{dt}$; de Bremond d'Ars et al., 1995). The theory has been tested and verified experimentally and numerically for viscosity ratios up to $\varepsilon = \mathcal{O}(10^2)$ (de Bremond d'Ars et al., 1995; Whitehead & Luther, 1975).

Equations (1) and (2) assume that both layers are horizontally infinite, but for a finite domain, for sufficiently large h and ε, the theoretical fastest-growing wavelength, λ_c, will be greater than the extent of the layers and so is not physically possible. Whether the domain is finite or infinite, all perturbations of all wavelengths will grow but the instability will develop with the wavelength that grows fastest. So we need to consider the growth rate of all modes with wavelengths equal to or smaller than the horizontal extent of the layers. In general the growth rate of a mode with wavelength λ and dimensionless wave number $K = \frac{4\pi h}{\lambda}$ is (Whitehead & Luther, 1975):

$$n = \frac{g \Delta \rho h}{K \mu_1} \left[\frac{\cosh K - 1 + \varepsilon(\sinh K - K)}{\sinh K + K + 2\varepsilon \cosh K + \varepsilon^2(\sinh K - K)} \right]. \tag{3}$$

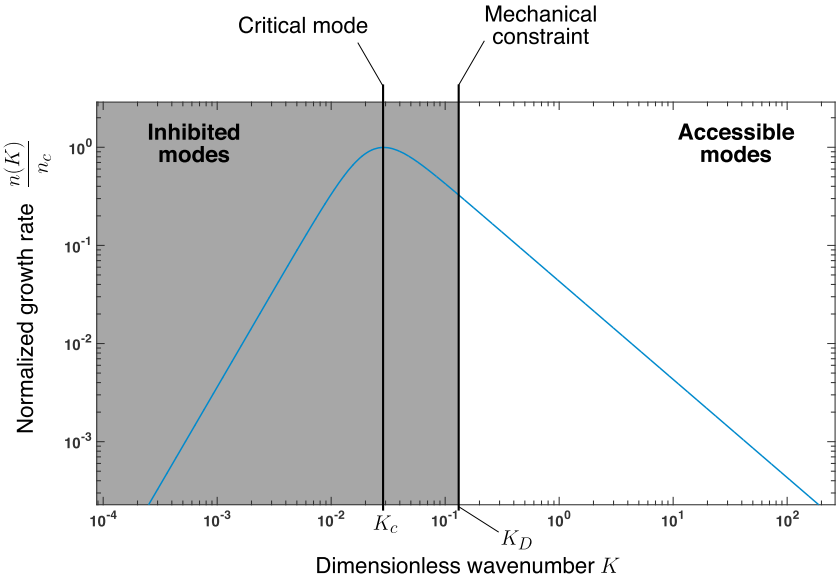

Figure 2. Normalized growth rate $\frac{n(K)}{n_c}$ as a function of dimensionless wave number K, for $\varepsilon = 10^6$. Any mode with $K < K_D$(gray area) cannot form because its wavelength is greater than the diameter of the container. As an example we illustrate this for $K_D = 0.13$, which corresponds to $\frac{h}{D} = 0.01$. For this case, the critical mode (K_c) cannot form. For large K, $\frac{n(K)}{n_c} = \frac{1}{0.232}\varepsilon^{-1/3}K^{-1} = 0.0431K^{-1}$ (see text for details).

The normalized function $\frac{n(K)}{n_c} = \frac{\varepsilon^{2/3}}{0.232K}\left[\frac{\cosh K - 1 + \varepsilon(\sinh K - K)}{\sinh K + K + 2\varepsilon\cosh K + \varepsilon^2(\sinh K - K)}\right]$ is plotted in Figure 2 for $\varepsilon = 10^6$. It reaches a maximum at $K_c = \frac{4\pi h}{\lambda_c}$, such that $n(K_c) = n_c$ (equation (2)). For $K \gg K_c$ and $\varepsilon \gg 1$, the growth rate decreases with increasing K, according to

$$\frac{n(K)}{n_c} \approx \frac{1}{0.232\varepsilon^{1/3}}K^{-1}. \tag{4}$$

If the RT instability occurs in a container with horizontal dimension $D < \lambda_c$, the tank walls will prevent the growth of all modes with $K < K_D = \frac{4\pi h}{D}$. Graphically, any mode within the gray shaded area in Figure 2 is inaccessible. Thus, in the presence of lateral boundaries with $K_D > K_c$ (i.e., $\lambda_c > D$), the fastest allowed growth rate is $n(K_D)$. It is useful to define a confinement parameter $\beta = \frac{\lambda_c}{D}$, such that the system is confined for $\beta > 1$. Using the definitions of β and λ_c, we can rewrite $K_D = 2.88\beta\varepsilon^{-1/3}$, therefore yielding

$$n(K_D) = \frac{n_c}{0.668\beta} = \frac{\Delta\rho g D}{4\pi\mu_2}. \tag{5}$$

This suggests that, in the case of a laterally confined RT instability, the growth rate is independent of both the thin layer thickness h and the viscosity ratio ε, though equation (5) requires experimental validation.

2.2. Are Mush-Melt Systems Confined?

The application of equations (1) and (2) to magmatic systems requires that melt layers can be considered horizontally infinite. To assess the condition for which this assumption is valid, we compute the confinement parameter $\beta = \frac{\lambda_c}{D}$ for natural magmatic systems. A system will be confined (or "clipped"; Burgisser & Bergantz, 2011) for $\beta > 1$, but it can be considered unconfined when $\beta \leq 1$.

We examine the confinement of three example scenarios: (a) a silicic, (b) an andesitic, and (c) a basaltic system, with viscosities and densities as indicated in Table 1. For each of the three systems, we calculate β for a range of melt layer widths (diameters if a circular lens) $500 \leq D \leq 2\cdot10^4$ m and heights $0.1 \leq h \leq 1,000$ m (Figure 1), which encompass typical values assumed in theoretical models (e.g., Annen et al., 2015; Bachmann & Bergantz, 2004) and consistent with estimates from geophysical surveys of natural systems (e.g., Lees, 1992; Tarasewicz et al., 2012). The majority of mush-melt systems are laterally confined (Figure 3). In fact, for the rheologies explored (Table 1), even an extremely wide ($D = 20$ km) layer of silicic (viscous) melt would be confined if thicker than 4 m. This result suggests that we should not simply apply equations (1) and (2) to typical lenses

Table 1
Parameters Used for a Silicic, an Andesitic, and a Basaltic System

Symbol	Description	Value used			Unit
–	–	Silicic	Andesitic	Basaltic	–
μ_1	Melt shear viscosity	10^5	$3 \cdot 10^2$	10	Pa·s
μ_2	Mush shear viscosity	10^{14}	10^{14}	10^{14}	Pa·s
ϵ	Viscosity ratio	10^9	$3 \cdot 10^{11}$	10^{13}	–
ρ_1	Melt density	2,300	2,500	2,800	kg/m^3
$\Delta\rho$[a]	Density difference	300	300	300	kg/m^3

Note. μ_1, Scaillet et al. (1998) & Murase and McBirney (1973); μ_2, Lejeune and Richet (1995) & Caricchi et al. (2007); ρ_1, Murase and McBirney (1973) & Annen et al. (2006); $\Delta\rho$, Whitney and Stormer (1985).
[a]We keep $\Delta\rho = 300$ kg/m^3 constant as density variations are negligible compared to viscosity variations.

in magma mushes because the mechanical constraints from the side boundaries will prevent the growth of the critical mode with wavelength λ_c. Instead, we expect the dynamics of the confined RT instability to be given by the fastest mode whose wavelength fits within the layer width. Therefore, we need a modified theory for RT instability that accounts for wall effects.

3. Materials and Methods

3.1. Fluids

To model mush-melt RT instabilities, we perform high viscosity contrast and laterally bounded experiments in cylindrical tanks, at low Reynolds number. We use glucose syrup (42DE-GL0106 from Ragus) as our viscous fluid and aqueous potassium carbonate (K_2CO_3) solutions as our low-viscosity fluids. Physical properties of these two fluids are summarized in Table 2 at both 18 and 8°C. Both fluids are Newtonian, and viscosity ratios in our experiments are in the interval $4.7 \cdot 10^4 \leq \epsilon \leq 2.2 \cdot 10^5$, a range which extends previous experimental data to much higher ratios.

Viscosity measurements were performed on a HAAKE RheoStress 1 rheometer (Thermo Fisher Scientific), with a concentric cylinders sensor system. Glucose viscosity at 8°C was too high to be measured directly as the rheometer was not calibrated to such high values. Instead, we measured viscosity from 18 to 28° C, and, assuming an Arrhenius model, we fitted an exponential curve through these data and extrapolated it down to 8°C. We measured glucose density via Archimedes' principle, by weighing a calibrated 10-cm^3 sinker (Mettler Toledo) in both air and glucose. The very low viscosity of the K_2CO_3 solutions allowed us to measure density by weighing 200 ml of solution in a volumetric flask.

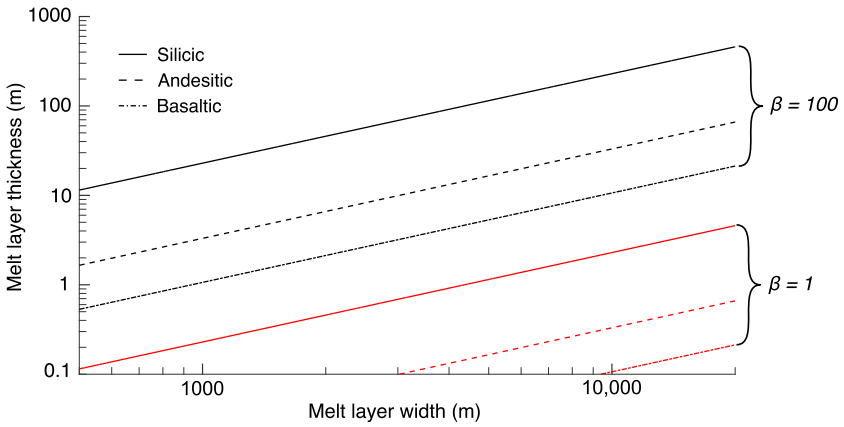

Figure 3. Confinement factor for a silicic, an andesitic, and a basaltic system. The red lines indicate where $\beta = 1$, whereas the black lines show $\beta = 100$. The systems are confined for $\beta > 1$.

Table 2
Density and Viscosity of the Glucose Syrup and the Potassium Carbonate Solutions Used at 8 and 18° C

Fluid	Density (kg/m^3)		Viscosity (Pa·s)	
	8° C	18° C	8° C	18° C
Glucose syrup	1,450 ± 5	1,435 ± 5	1,530–2,000	300–480
K_2CO_3 solution	1,440–1,550 ± 1		0.009 ± 0.001	0.007 ± 0.001

3.2. Experimental Methods

We use two tank sizes to investigate the effect of lateral confinement. All tanks are made of transparent Perspex and are cylindrical to avoid corner effects.

3.2.1. Narrow Tank Experiments

The narrowest tanks have a diameter $D = 5.00 \pm 0.02$ cm and height $H = 40.00 \pm 0.05$ cm (Figure 4). Three tanks of this geometry were made in order to efficiently run concurrent experiments. The confinement factors ($\beta = \frac{\lambda_c}{D}$) for experiments in these tanks are $10 \leq \beta \leq 210$; hence, wall effects are likely to be very important in all experiments with $D = 5$ cm.

We conducted experiments in two temperature-controlled rooms, at 18°C (laboratory) and 8°C (cold room), to sample a wider range of viscosity ratios. We first pour more than 30 cm of glucose syrup into the tank, cover the top of the tank, and leave it to rest until all the air bubbles have escaped. The uppermost part of the syrup usually dehydrates and stiffens. We thus remove this stiff layer a few minutes before starting the experiment. This is long enough for the disturbed interface to flatten but short enough to avoid significant drying. The experiment is started by delicately pouring dyed K_2CO_3 solution on top of the glucose layer. Pouring takes a few seconds, which is much faster than the time for an RT instability to develop (always >3 min). This configuration (viscous fluid underneath) is flipped compared to magmatic systems with a buoyant lens under a more viscous mush. Nonetheless, the dynamics of the instability will be identical because the driving force, buoyancy, is independent of which fluid is on top of the other; only the density difference $\Delta\rho$ is important (Whitehead & Luther, 1975). All experiments are recorded with a fixed camera.

In most experiments, there is air directly above the K_2CO_3 solution, forming a free-slip BC above. To check the influence of the BC, we repeated some experiments with a no-slip upper BC by placing a circular perspex lid on top of the K_2CO_3 layer just after pouring it. The lid diameter is 0.4 mm less than the tank to allow air escape during placement.

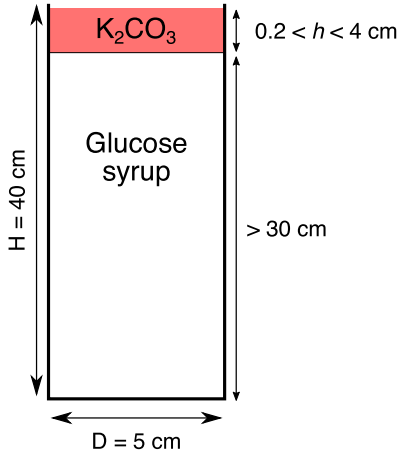

Figure 4. Diagram of a narrow tank experimental setup.

3.2.2. Wide Tank Experiments

We perform similar experiments in a wide tank with diameter $D = 28.70 \pm 0.05$ cm and height $H = 39.20 \pm 0.05$ cm, achieving $1.2 \leq \beta \leq 6.9$. Although $\beta > 1$, we expect wall effects to be small and our results to approach the theoretical predictions of Whitehead and Luther (1975). The experimental procedure is identical to the narrow tank case, with the exception that we pour the K_2CO_3 solution through a nozzle with seventy-two 1.5-mm-diameter holes to reduce disturbance of the interface. Again, we conduct experiments at both 18 and 8°C. We, however, did not run any no-slip upper BC experiment with the wide tank.

3.3. Linear Stability Analysis

To complement our experimental investigation, we perform an linear stability analysis (LSA), based on the work of Sweeney et al. (2013). They theoretically investigated RT instabilities in a narrow, finite cylinder (no-slip BC), but their published results cannot be directly applied to our scenario for two reasons. First, they only examined cases where the two fluid layers have equal thicknesses, and second the viscosity ratios considered are too low ($\varepsilon \leq 10^2$). We use their numerical routines to reproduce our experimental conditions and to extend results to higher β values than achieved in the laboratory. Full technical details can be found in Sweeney et al. (2013).

Table 3
Summary of Experiments Performed and Corresponding Linear Stability Analysis Results in Order of Increasing β

Exp	$\Delta\rho$	$\frac{\mu_2}{\mu_1}$	h	β	$\frac{n_c}{n_{obs}}$	Comment	$\frac{n_c}{n_{obs}}$
–	($\pm$5 kg/m^3)	–	($\pm$0.05 cm)	–	(Exp)	–	(LSA)
46	6	66,000 $\pm$ 5,000	0.2	1.2 $\pm$ 0.3	1.2 $\pm$ 1.0	Wide Tank	1.8
45	22	220,000 $\pm$ 14,000	0.2	1.8 $\pm$ 0.4	1.9 $\pm$ 0.7	Wide Tank	2.2
41	12	55,000 $\pm$ 5,000	1.2	6.9 $\pm$ 0.4	4.0 $\pm$ 1.8	Wide Tank	7.7
4	50	53,000 $\pm$ 5,000	0.3	10 $\pm$ 2	15 $\pm$ 3		11
15	15	53,000 $\pm$ 5,000	0.3	10 $\pm$ 2	14 $\pm$ 6		11
39	67	66,000 $\pm$ 5,000	0.3	10 $\pm$ 2	10 $\pm$ 2	No slip	12
31	65	66,000 $\pm$ 5,000	0.5	18 $\pm$ 2	19 $\pm$ 3		20
14	35	53,000 $\pm$ 5,000	0.8	26 $\pm$ 2	28 $\pm$ 5		29
5	50	53,000 $\pm$ 5,000	0.8	26 $\pm$ 2	33 $\pm$ 5		29
20	50	53,000 $\pm$ 5,000	0.8	26 $\pm$ 2	30 $\pm$ 4		29
21	12	66,000 $\pm$ 5,000	0.8	26 $\pm$ 2	21 $\pm$ 9		29
38	44	66,000 $\pm$ 5,000	0.8	28 $\pm$ 2	36 $\pm$ 6	No slip	38
42	52	220,000 $\pm$ 14,000	0.6	31 $\pm$ 3	24 $\pm$ 3	No slip	35
25	50	66,000 $\pm$ 5,000	1	35 $\pm$ 2	46 $\pm$ 6		39
7	15	53,000 $\pm$ 5,000	1.4	46 $\pm$ 2	40 $\pm$ 14		51
8	15	53,000 $\pm$ 5,000	1.4	46 $\pm$ 2	43 $\pm$ 15		51
13	35	53,000 $\pm$ 5,000	1.4	46 $\pm$ 2	60 $\pm$ 9		51
22	50	66,000 $\pm$ 5,000	1.3	46 $\pm$ 2	62 $\pm$ 7		51
44	12	47,000 $\pm$ 5,000	1.6	50 $\pm$ 3	49 $\pm$ 21	No slip	56
27	67	66,000 $\pm$ 5,000	1.6	56 $\pm$ 2	68 $\pm$ 7		63
9	15	53,000 $\pm$ 5,000	2	65 $\pm$ 2	52 $\pm$ 18		73
3	50	53,000 $\pm$ 5,000	2	66 $\pm$ 3	49 $\pm$ 7		73
2	116	53,000 $\pm$ 5,000	2	66 $\pm$ 3	65 $\pm$ 8		73
12	17	166,000 $\pm$ 11,000	1.4	67 $\pm$ 3	61 $\pm$ 19		75
11	30	166,000 $\pm$ 11,000	1.6	77 $\pm$ 3	85 $\pm$ 15		86
30	60	66,000 $\pm$ 5,000	2.3	81 $\pm$ 3	120 $\pm$ 13		90
35	44	66,000 $\pm$ 5,000	2.3	81 $\pm$ 3	113 $\pm$ 15	No slip	90
40	52	220,000 $\pm$ 14,000	1.7	89 $\pm$ 3	65 $\pm$ 7	No slip	99
19	50	166,000 $\pm$ 11,000	1.9	91 $\pm$ 3	61 $\pm$ 8		102
28	65	220,000 $\pm$ 14,000	1.8	94 $\pm$ 3	88 $\pm$ 8		105
36	53	220,000 $\pm$ 14,000	2	105 $\pm$ 3	109 $\pm$ 15		117
18	12	75,000 $\pm$ 10,000	3.1	114 $\pm$ 6	100 $\pm$ 45		127
32	52	220,000 $\pm$ 14,000	2.3	121 $\pm$ 4	98 $\pm$ 11		134
43	52	220,000 $\pm$ 14,000	2.4	126 $\pm$ 4	110 $\pm$ 13	No slip	140
6	12	53,000 $\pm$ 5,000	4	131 $\pm$ 5	87 $\pm$ 38		146
37	51	220,000 $\pm$ 14,000	2.7	142 $\pm$ 4	121 $\pm$ 13		158
29	65	220,000 $\pm$ 14,000	2.9	152 $\pm$ 4	155 $\pm$ 14		170
33	52	220,000 $\pm$ 14,000	2.9	152 $\pm$ 4	164 $\pm$ 18		170
24	50	220,000 $\pm$ 14,000	3.4	178 $\pm$ 4	151 $\pm$ 16		199
26	59	220,000 $\pm$ 14,000	4	210 $\pm$ 5	278 $\pm$ 26		234

Note. All symbols are defined in the text. Unless indicated by "Wide Tank", all experiments were performed in a narrow tank with $D = 5.00 \pm 0.02$ cm. The final column indicates $\frac{n_c}{n_{obs}}$ for n_c calculated by equation (2) and n_{obs} determined by linear stability analysis.

Table 4
Summary of Parameters Used in the Additional Linear Stability Analysis Performed and Resulting Growth Rates

D (cm)	h (cm)	ε	β	$\frac{n_c}{n_{obs}}$
100	2.5	10^4	2.3	3.05
100	3.75	10^4	3.5	4.34
100	5	10^4	4.7	5.67
100	6.25	10^4	5.9	7.01
100	7.5	10^4	7.0	8.35
2	2.3	10^6	500	560
2	4.6	10^6	1,000	1,180
1	4.6	10^6	2,000	2,230
1	9.2	10^6	4,000	4,470
1	11.5	10^6	5,000	5,590
1	18.5	10^6	8,000	9,120
1	23	10^6	10,000	11,280

Note. We kept $\Delta\rho = 50$ kg/m^3 constant in all the runs. Results are plotted as "Complementary LSA" in Figure 7.

4. Results

We conducted a total of 40 experiments, sampling the range $1.2 \leq \beta \leq 210$. The viscosity ratios ($4.7 \cdot 10^4 \leq \varepsilon \leq 2.2 \cdot 10^5$) are more than 2 orders of magnitude higher than previous large viscosity contrast RT experiments (e.g., de Bremond d'Ars et al., 1995; Huppert et al., 1984). A summary of the experimental parameters and corresponding results is presented in Table 3. We performed an LSA for each set of experimental parameters (Table 3). To complete and extend our data set, we also carried out LSA in the ranges $2.3 \leq \beta \leq 7.0$ and $500 \leq \beta \leq 10,000$, with sets of parameters that have not been or could not be experimentally investigated. The conditions and results for these additional LSA runs are summarized in Table 4. We thus obtain theoretical growth rates for the confined RT instabilities considered, which can be compared to our experimental observations and to unconfined theory.

Figure 5 shows the time series of two typical experiments in a narrow tank: one at room temperature with air above (Figure 5a) and one at 8° C with a no-slip upper BC (Figure 5b). Regardless of the tank size or the BC, the overall dynamics are similar. First, a single, small protrusion of K_2CO_3 solution forms at the interface between the two fluids. The protrusion grows into an ellipsoidal to spheroidal pocket of solution. When all of the initial

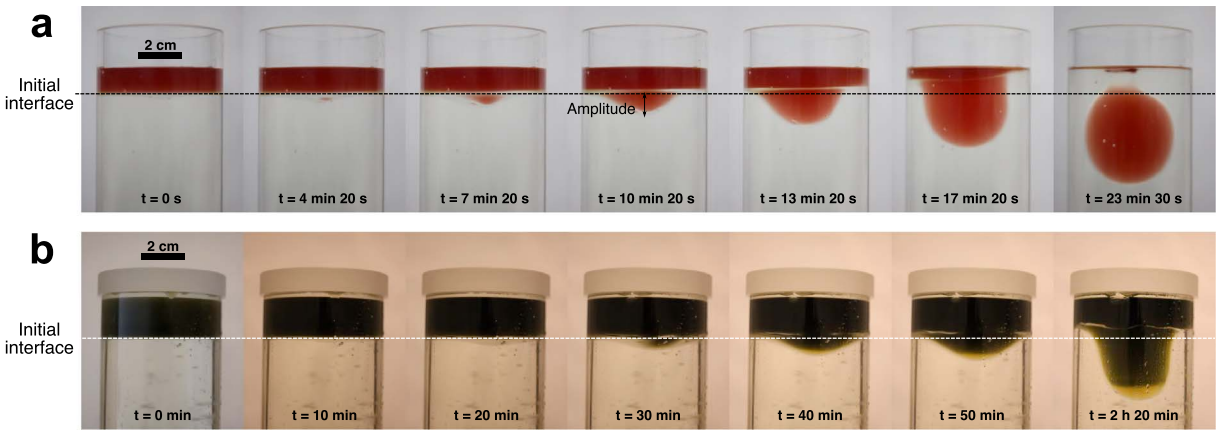

Figure 5. Time series of the initial stage of (a) experiment 25, at 18° C with $h = 1$ cm, $\Delta\rho = 50$ kg/m^3, $\varepsilon = 6.6 \cdot 10^4$, and $\beta = 35$ and (b) experiment 40, at 8° C with $h = 1.7$ cm, $\Delta\rho = 52$ kg/m^3, $\varepsilon = 2.2 \cdot 10^5$, $\beta = 89$ and a no-slip boundary condition. The initial interfaces are highlighted and an example of how amplitude is measured is provided.

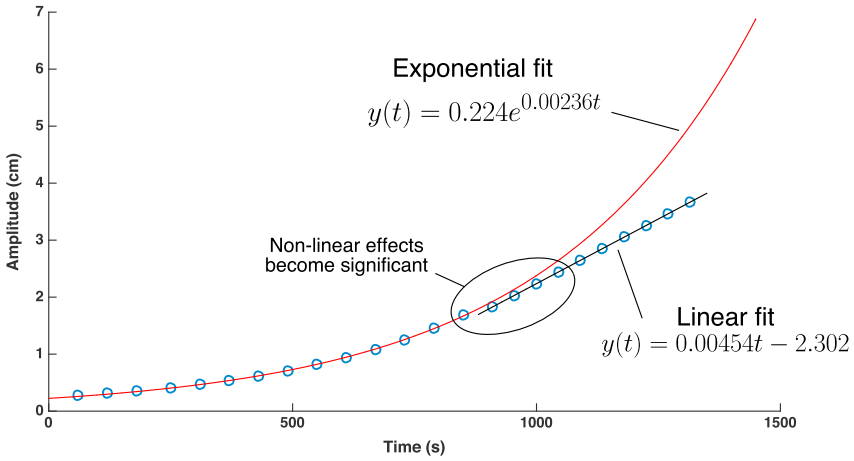

Figure 6. Amplitude of the perturbation as a function of time for experiment 25 (Figure 5a). An exponential curve is fitted through the first data points and a line is fitted through the last ones. Equations of best fit are provided.

volume has been drawn into this spheroid, it sinks as a single pocket of fluid. The dimensions of this pocket of fluid stay constant, until it reaches the bottom of the tank.

The location of the initial protrusion is sensitive to asperities on the syrup surface or disturbance induced by pouring the K_2CO_3 solution; hence, the protrusion is sometimes initially slightly off centered (Figure 5b for instance). Replicate experiments show that these deviations do not significantly affect the results: The growth rate of the protrusion is similar, and the K_2CO_3 solution layer always becomes thickest near the center of the tank well before it evolves into a spheroid sinking through the syrup.

The amplitude of the perturbation, defined as the vertical distance from the initial liquid-liquid interface location to the bottom of the protrusion (see Figure 5a), was measured as a function of time for each experiment (Figure 6). For all experiments there is an initial exponential increase in amplitude before transitioning to linear growth. This transition corresponds to the stage at which linearized stability theory (e.g., Whitehead & Luther, 1975) is no longer valid. We therefore obtain an exponential fit of the form $y(t) = Ae^{n_{obs}t}$ for the initial growth of each experiment. The n_{obs} parameter in the exponential then corresponds to the growth rate of our experimental RT instability and can be compared to theoretical unconfined predictions.

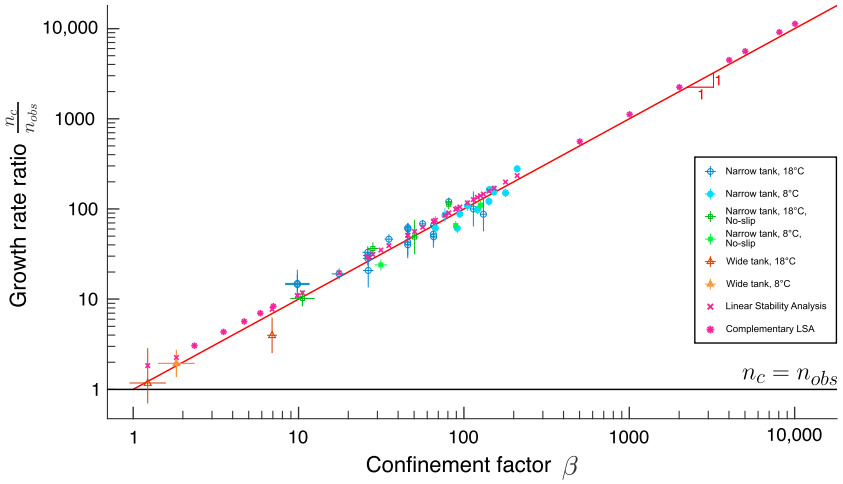

Figure 7. Ratio of theoretical unconfined growth rates n_c from Whitehead and Luther (1975) to our experimental and analytical confined growth rates n_{obs} as a function of confinement parameter β. The red line represents $\frac{n_c}{n_{obs}} = \beta$ and the horizontal black line indicates $n_c = n_{obs}$. The symbol and color code is used to distinguish different experimental conditions. The crosses represent linear stability analysis (LSA) results reproducing experimental conditions whereas the stars show complementary LSA runs which have no experimental counterpart (Table 4).

Figure 7 displays the ratio $\frac{n_c}{n_{obs}}$ as a function of the confinement parameter β for both experiments and LSA, where n_c is the theoretical unbounded critical growth rate from equation (2). The no-slip experiments are indistinguishable from the free-slip ones, indicating that the top BC only has a minor influence on the growth rate. Both the experimental and analytical results follow a linear trend of $\frac{n_c}{n_{obs}} \approx \beta$, although for $\beta \lesssim 10$, the slope of the LSA data trend decreases. The linear best fit through the experimental data is $\frac{n_c}{n_{obs}} = (0.93 \pm 0.03)\beta + (0.15 \pm 0.07)$. Similarly, a fitted line through the LSA points for $\beta > 10$ is $\frac{n_c}{n_{obs}} = (1.0009 \pm 0.0002)\beta + (0.0454 \pm 0.0005)$.

In summary, our results show that bounded growth rates (n_{obs}) are reduced compared to the unbounded theoretical values (n_c) by approximately a factor of β. For simplicity, in our applications to magmatic system we take $\frac{n_c}{n_{obs}} = \beta$, which is within 10% of the lines of best fit to our data (Figure 7) and introduces negligible error compared to the uncertainties on the magma and mush properties that affect RT instabilities.

5. Discussion

5.1. Confined RT Instability Dynamics

Our experimental results with $1.2 \leq \beta \leq 210$ and $4.7 \cdot 10^4 \leq \varepsilon \leq 2.2 \cdot 10^5$ demonstrate that the dynamics of a confined RT instability is qualitatively similar to the unconfined case. Indeed, the instability starts with an exponential growth, followed by a linear growth (e.g., Figure 6), a phenomenon well documented for the unbounded case (e.g., Waddell et al., 2001). Moreover, the shape of the perturbations is similar to previous experimental studies (e.g., Waddell et al., 2001; Whitehead & Luther, 1975; Wilkinson & Jacobs, 2007). Our instabilities differ from the unbounded case because only a single protrusion forms, as opposed to multiple, uniformly spaced bulges, as observed by Whitehead and Luther (1975) and de Bremond d'Ars et al. (1995) for instance.

Our experimental and analytical results indicate that as β approaches unity, there is a transition in the instability growth rate from $\frac{n_c}{n_{obs}} = \beta$ when the system is bounded towards $n_c = n_{obs}$, characteristic of an unbounded ($\beta \ll 1$) system (i.e., n_{obs} matches the theoretically predicted value for a laterally infinite system). Based on these results, we estimate a characteristic RT instability timescale, that is, the time for the instability amplitude to increase by a factor of e (≈ 2.72), by

$$\tau_{RTI} = \begin{cases} \frac{1}{n_c} = \frac{\mu_2}{0.232 g \Delta\rho h} \varepsilon^{-1/3} & \text{if } \beta \leq 1, \\ \frac{\beta}{n_c} = \frac{6\pi\mu_2}{\Delta\rho g D} & \text{if } \beta > 1. \end{cases} \tag{6}$$

In contrast to the unbounded case, the confined timescale does not depend on either the initial layer thickness h or the viscosity ratio ε because the instability wavelength is set by D. Rather, the controlling parameters are the diameter of the layer D, the viscosity of the upper layer μ_2, and the density contrast between the fluids $\Delta\rho$. Comparing equations (5) and (6), we notice that our experimental growth rates are a factor of 3/2 slower than estimated with the linear stability theory of Whitehead and Luther (1975) for $\lambda = D$. This is most likely because the tank walls add a no-slip BC (i.e., will exert significant drag on the fluids) that is not accounted for in equation (5).

5.2. Application to Igneous Systems

There are multiple mechanisms where buoyant layers can form within igneous mush systems. One mechanism is by replenishment with new magma spreading out within or at the base of a mush. Initially, the new magma layer may intrude as a denser layer at the base of the reservoir or at its neutral buoyancy level within the reservoir. In either case the magma layer may become less dense with time by, for example, crystallization and differentiation with dense components segregating to the base of the flow. Volatile exsolution can also increase the buoyancy of the layer (Huppert et al., 1982). Additionally, the overlying mush may be heated from below (e.g., Burgisser & Bergantz, 2011; Couch et al., 2001) or be fluxed by volatiles released from the replenishing magma layer (Bachmann & Bergantz, 2006) to develop a zone of reduced density. Another mechanism of layer formation is through dynamic melt percolation due to mush compaction, which can result in formation of melt-rich regions. One-dimensional models of porous media flow and compaction predict the development of multiple melt-rich regions (e.g., Jackson et al., 2003; Solano et al., 2012). Intrinsically, 1-D models cannot include RT instabilities of growing melt layers. Likewise, exsolved magmatic volatiles can migrate through mushes and accumulate as fluid layers (Christopher et al., 2015). Each of the above scenarios

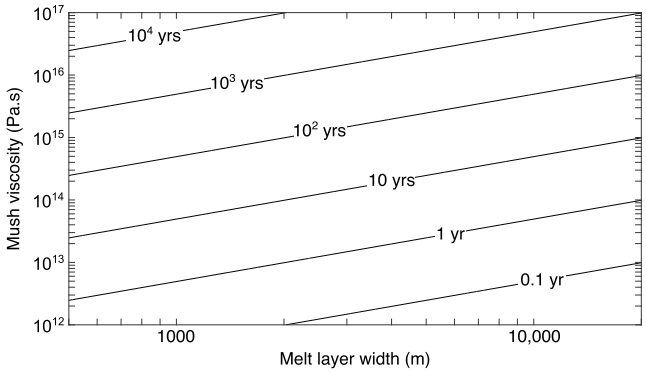

Figure 8. Confined Rayleigh-Taylor instability timescale as a function of melt layer diameter and mush viscosity.

for melt- or fluid-layer generation could be modeled individually and in detail, but this is beyond the scope of the current paper. Here we investigate the stability of buoyant magma layers of fixed thickness or growing at a fixed rate to provide a first-order understanding of the likely timescales and length scales that can be expected. Our analysis is restricted to RT instablities; we have not explored the potential importance of melt-mush flow mechanisms and smaller-scale instabilities related to the porous or brittle nature of the mush, which could develop along with or instead of RT instabilities (e.g., Connolly & Podladchikov, 2013; Oppenheimer et al., 2015; Sandnes et al., 2011; Schmeling et al., 2017; Scott & Stevenson, 1984, 1986).

Figure 8 presents estimates of confined RT instability timescales for a range of mush viscosities μ_2 and melt layer diameters (or widths if not circular) D relevant to igneous systems. We use the instability timescale defined in equation (6), with β calculated as λ_c/D using λ_c defined in equation (1), and physical parameter values listed in Table 1. The wide range of calculated timescales (10^1–10^4 years) match the variability of timescales observed for volcanic processes, from small and frequent events to large and rare events (e.g., caldera forming eruptions). On the other hand, the very long timescales involved with the slowest instabilities imply that other processes (e.g., solidifaction by cooling) could occur faster and inhibit the onset of RT instability.

5.2.1. Comparison to Cooling Timescale

First, we consider a case where there is a strong temperature difference between the melt and the mush and compare our RT instability timescale to a characteristic cooling timescale. Such a scenario could occur when a cold mush system is replenished by hot magma from depth. In this case, if the cooling timescale is shorter than the RT instability timescale, the melt layer will freeze before an instability can develop. For simplicity, we assume cooling occurs via conduction only and define a characteristic cooling timescale $\tau_{\text{cool}} = \frac{h^2}{\kappa}$, where h is the melt layer thickness and κ is the thermal diffusivity. We use $\kappa = 6 \cdot 10^{-7}$ m^2/s (Annen et al., 2006; Romine et al., 2012; Whittington et al., 2009).

Figure 9 shows the lines where $\tau_{\text{cool}} = \tau_{\text{RTI}}$ as h and D are varied and for two mush viscosities. Above these lines, RT instabilities have time to develop, whereas under the lines, the melt layer will freeze before the instability develops significantly. The results are dramatically different depending on which mush viscosity is considered. For a melt-rich mush ($\mu_2 = 10^{13}$ Pa·s), RT instabilities develop sufficiently quickly that the required thickness for the instability to develop faster than conductive cooling is only 1.4–8.9 m, depending upon the layer diameter. This range, however, becomes 140–900 m for a near-solidus mush ($\mu_2 = 10^{17}$ Pa·s). The mush rheology therefore exerts a critical control on the necessary thickness to develop instability and hence the volume of eruptible material ascending through the mush as a result of the instability.

This simple analysis omits two potentially important but opposing mechanisms: (a) we only consider cooling via conduction and ignore convection, which can speed up cooling, and (b) the hot intrusion can reheat the mush, thus decreasing its viscosity and speeding up RT development. To get some insight about when convection may occur, we calculate the Rayleigh number $\text{Ra} = \frac{g\rho_1\alpha\Delta T h^3}{\kappa\mu_1}$, where α is the thermal expansion of the melt and ΔT is the temperature difference between the melt and the mush. We use $\alpha = 5 \cdot 10^{-5}$ K^{-1} and $\Delta T = 100$ K and densities and viscosities for the three compositions considered in Table 1 (e.g., Bachmann & Bergantz, 2006; Degruyter & Huber, 2014; Huber et al., 2010; Jackson et al., 2003). Taking $\text{Ra} = 27\frac{\pi^4}{4} \approx 657.5$

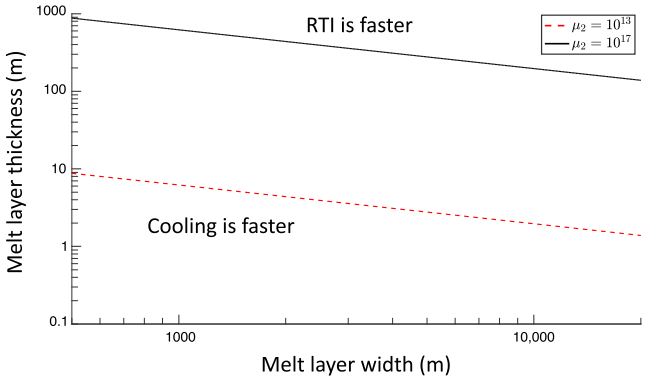

Figure 9. Isolines $\tau_{cool} = \tau_{RTI}$ as a function of melt layer width and thickness and for two mush viscosities. Above these lines, there is sufficient time for the Rayleigh-Taylor instability (RTI) to grow, whereas under the lines, the melt layer will freeze before the instability develops significantly.

as the critical value for the onset of convection (Turcotte & Schubert, 1982), this calculation suggests that all the layers previously considered would convect, except for extremely thin silicic layers ($h < 49$ cm). Therefore, the cooling timescale could be faster than assumed in Figure 9, which would raise the $\tau_{cool} = \tau_{RTI}$ lines to greater h for a given D. Concerning reheating of the mush, Burgisser and Bergantz (2011) showed that RT instabilities could lead to significant mush overturn ("unzipping"), yet their analysis is restricted to low mush viscosities ($\mu_2 = 10^6 - 10^{12}$ Pa·s) and considers high temperature differences ($\Delta T = 45$–500 K). Therefore, the importance of this mechanism has yet to be tested for our scenario.

5.2.2. Comparison to Accumulation Timescale

The previous discussion assumes that melt accumulation into a layer occurs much faster than the instability timescale, such that a melt lens of any thickness is a feasible starting condition for considering RT instabilities. Next, we relax this assumption and explore the relation between melt accumulation and RT instability timescales.

De Bremond d'Ars et al. (1995) investigated the case of a horizontally extensive buoyant layer that thickens and a constant rate, $\dot{h} = \frac{dh}{dt}$. They showed that blobs of buoyant fluid form and rise away from the base when the layer growth rate $\frac{\dot{h}}{h}$ and the instability growth rate $\frac{1}{\tau_{RTI}}$ are equal. For the formation of a new layer (i.e., starting with $h = 0$), the layer growth rate $\frac{\dot{h}}{h}$ is initially very large and then monotonically decreases as h increases. Thus, for any given melt input rate $\dot{h}$, there exists a maximum layer thickness beyond which melt will be removed faster via RT instabilities than it is added. We can estimate this thickness, the corresponding magma volume, and the time required to assemble it for a range of parameters. First, we calculate the time at which $\frac{\dot{h}}{h} = \frac{1}{\tau_{RTI}}$. We can then compute the layer thickness using the constant melt input rate and corresponding volume, assuming a cylindrical shape. We use the same criterion as de Bremond d'Ars et al. (1995) but account for lateral confinement when relevant.

Figure 10 shows the accumulation time and associated melt volume for a silicic melt under a melt-rich mush ($\mu_2 = 10^{13}$ Pa·s; Figure 10a) and a near-solidus mush ($\mu_2 = 10^{17}$ Pa·s; Figure 10b), as a function of the layer diameter D and the melt input rate $\dot{h}$. The chosen range of input rates $\dot{h}$ span values from magma accumulation models and field studies (e.g., Karakas et al., 2017; White et al., 2006). The kinks in the lines for melt input rates of $\dot{h} = 0.1, 1, 10$ m/year in Figure 10a correspond to the transition from confined to unconfined instability regime with increasing D. For conditions where the RT instability is not confined (i.e., $\lambda < D$), the accumulation times are independent of D but depend on $\dot{h}$ (forming horizontal lines in the upper panel of Figure 10a). In confined scenarios (some combinations of $\dot{h}$ and D in Figure 10a and all conditions plotted in Figure 10b), the accumulation times are independent of $\dot{h}$, hence the collapse into a single line for a given μ_2. The choice of mush viscosity has a major impact on the results and allows us to recover a large range of timescales (0.3–$4 \cdot 10^4$ years). The corresponding volumes range from 10^5 up to 10^{12} m^3.

Our calculations suggest that RT instabilities could play an important role in controlling the size and frequency of volcanic events. A working hypothesis is that volcanic eruptions and episodes of volcanic unrest are the consequences of these instabilities. The calculated timescales and volumes are comparable with natural

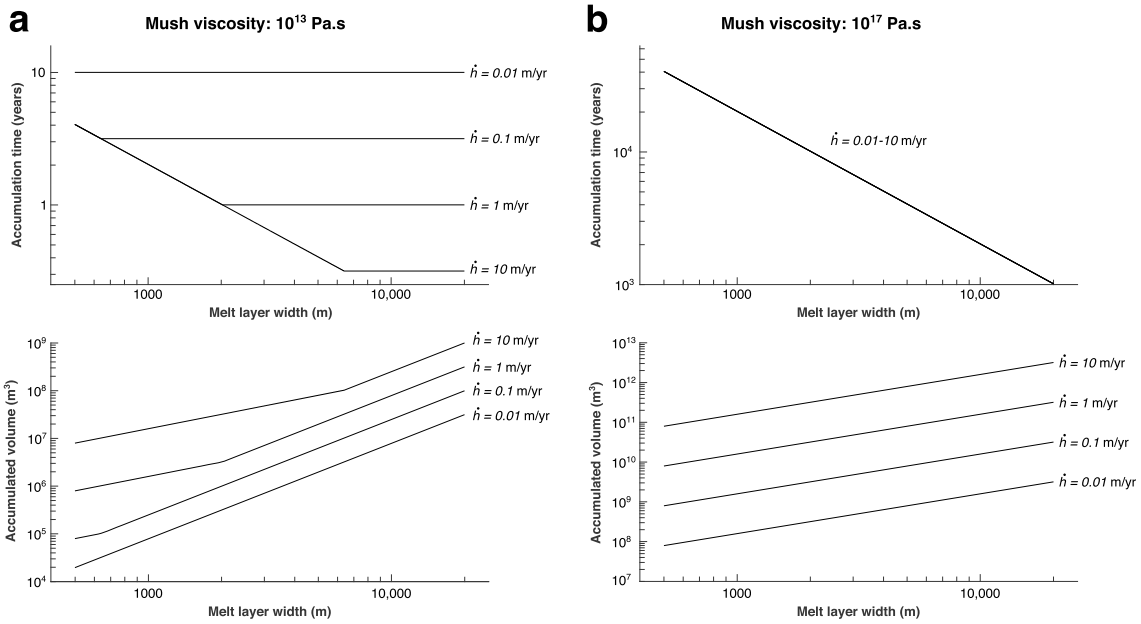

Figure 10. Time before the onset of instability and accumulated volume in the case of a linearly growing buoyant layer of silicic melt under (a) a melt-rich mush and (b) a near-solidus mush. The kinks in the lines in (a) for $\dot{h} = 0.1$, 1, and 10 m/year correspond to a change from confined to unconfined instability regime with increasing melt layer width. There are no kinks in (b) because for the higher mush viscosity, Rayleigh-Taylor instabilities are confined for the full range of scenarios plotted.

volcanic values (e.g., Pyle, 2015) and span the full range between small mafic eruptions (e.g., Strombolian type) to the largest magnitude eruptions (e.g., caldera-forming eruptions and flood basalts). The time needed for an instability to develop allows melt to accumulate in large layers and corresponds to a dormant period (e.g., Rougier et al., 2018; Sheldrake et al., 2016), whereas the instability may destabilize the system and produce a period of unrest or an eruption. Additionally, successive instabilities without eruption could yield larger accumulated volumes (e.g., Sparks & Cashman, 2017).

5.2.3. Crystal Mush Rheology

A limitation in the application of our experimental and theoretical results to natural systems is the assumption of Newtonian mush rheology. Our experiments involved Newtonian fluids, but natural crystal mushes are generally shear-thinning and may have a yield strength, that is, a minimum stress required for flow to occur (e.g., Hoover et al., 2001; Kerr & Lister, 1991; Saar et al., 2001). With Newtonian fluids, an RT instability will always develop in response to a denser fluid overlying a less dense fluid, although in some scenarios it will grow slowly enough that it can be neglected over the timescale of interest. The same is true of shear-thinning fluids; here the relevant viscosity for the early stage of the instability is the (high) viscosity in the limit of the shear rate approaching 0. With a yield strength, however, the buoyant force from the melt layer $\Delta\rho gh$ has to exceed the mush yield strength τ_0; otherwise, the mush will act as a solid (e.g., elastic) body, preventing the growth of the RT instability, akin to initiation of thermal convection of a fluid with a yield strength (Balmforth & Rust, 2009). True yield strengths (i.e., a minimum stress for any flow to occur) may not exist (e.g., Barnes, 1999); however, if the effective viscosity of a mush at low stresses is extremely large such that it has an apparent yield strength, then the instability will grow so slowly as to be negligible unless $\Delta\rho gh > \tau_0$.

We can estimate the minimum thickness required for an RT instability to develop when the mush has a yield strength as $h_{\min} = \frac{\tau_0}{\Delta\rho g}$. For mush yield strengths in the range $\tau_0 = 10^5$–10^6 Pa (Castruccio et al., 2013; Lejeune & Richet, 1995) and $\Delta\rho = 300$ kg/m^3, we find $h_{\min} = 34$–340 m. This crude estimate suggests that the required thickness to overcome a yield strength could be of the same order of magnitude as typical melt layer thicknesses. Mush strength could thus facilitate the accumulation of melt lenses by impeding RT instability development for the thinnest layers. This effect could be enhanced if crystals have grown together and bonded in a stagnant mush, producing a yield strength greater than 10^6 Pa.

6. Conclusion

Rayleigh-Taylor instabilities occur naturally in magmatic systems when buoyant melt (or magmatic volatile phase) is trapped underneath a denser crystalline mush. For a wide range of expected viscosities, the large viscosity contrast between the mush and melt lens means that the theoretical fastest-growing wavelength is unfeasibly large and so the wavelength of the instability is the largest available: the diameter of the lens. This lateral confinement means that the growth rate of the instability is reduced compared to the theoretical unconfined scenario. Importantly, if confined, the instability growth rate no longer depends on the thickness or viscosity of the lens; rather, it depends only on the diameter of the lens, the viscosity of the mush and the density contrast between the lens and mush. The thickness of the lens will, however, play a role if the mush has an apparent yield strength because the instability will only initiate if the buoyancy stress, which is proportional to the lens thickness, is sufficient to overcome the yield strength. Thickness also matters in scenarios where the melt is hotter than the mush, as thinner lenses will cool more quickly, allowing less time for RT instability development before the magma is too crystalline to flow.

A fully developed confined RT instability transforms the melt lens into a spheroid of melt, which ascends through the mush. A lens of melt can only exist if it thickens faster than melt is removed by a RT instability. So both the timescale for transforming a lens into a rising spheroid and the volume of the spheroid will depend on the rate of input of melt into the lens as well as its diameter, the viscosity of the mush, and the density contrast between the lens and mush. We postulate that RT instabilities may play a role in regulating the size and frequency of volcanic eruptions and volcanic unrest. Using feasible ranges of the relevant parameters, we calculate timescales and volumes that span small, frequent mafic eruptions to the largest and much rarer caldera-forming and flood basalt eruptions. Also, multiple episodes of layer instability without eruption can lead to accumulations of larger magma volumes and provide one explanation of volcanic unrest.

In a magmatic system composed of a vertically extensive mush containing multiple melt lenses, can the rise of a blob of melt or volatiles trigger a feedback to cause large-scale destabilitization? The growth rate of a laterally confined RT instability in a Newtonian mush does not depend on the thickness of the melt lens. So the ascent of a blob of melt into a more shallow lens will not cause an accelerated destabilization of that lens unless: (a) it causes the diameter of the lens to increase (and so increases the wavelength of the RT instability) or (b) it increases the thickness of the lens such that its buoyancy stress overcomes the yield strength of the mush above it. Mush rheology therefore is important for controlling where melt (and magmatic volatile phases) accumulate in layers, how much melt accumulates, and how frequently packets of melt are released.

Acknowledgments
We thank Rich Kerswell for providing and helping with his numerical tools. We also thank the Editor A. Revil and reviewers J. de Bremond d'Ars and A. R. Cruden for their insightful comments that have improved the manuscript; some of their points are beyond the scope of this paper but will influence our further research. This work was supported by NERC grant NE/P017371/1. All the data from experiments and linear stability analysis are presented in Tables 3 and 4.

References

Annen, C. J., Blundy, J. D., Leuthold, J., & Sparks, R. S. J. (2015). Construction and evolution of igneous bodies: Towards an integrated perspective of crustal magmatism. *Lithos*, *230*, 206–221. https://doi.org/10.1016/j.lithos. 2015.05.008

Annen, C. J., Blundy, J. D., & Sparks, R. S. J. (2006). The genesis of intermediate and silicic magmas in deep crustal hot zones. *Journal of Petrology*, *47*(3), 505–539. https://doi.org/10.1093/petrology/egi084

Bachmann, O., & Bergantz, G. W. (2004). On the origin of crystal-poor rhyolites: Extracted from batholithic crystal mushes. *Journal of Petrology*, *45*(8), 1565–1582. https://doi.org/10.1093/petrology/egh019

Bachmann, O., & Bergantz, G. W. (2006). Gas percolation in upper-crustal silicic crystal mushes as a mechanism for upward heat advection and rejuvenation of near-solidus magma bodies. *Journal of Volcanology and Geothermal Research*, *149*(1-2), 85–102. https://doi.org/10.1016/j.jvolgeores.2005.06.002

Bachmann, O., & Huber, C. (2016). Silicic magma reservoirs in the Earth's crust. *American Mineralogist*, *101*(11), 2377–2404. https://doi.org/10.2138/am-2016-5675

Balmforth, N. J., & Rust, A. C. (2009). Weakly nonlinear viscoplastic convection. *Journal of Non-Newtonian Fluid Mechanics*, *158*(1-3), 36–45. https://doi.org/10.1016/j.jnnfm.2008.07.012

Barnes, H. (1999). The yield stress—A review or '$\pi\alpha\nu\tau\alpha\rho\epsilon\iota$'—everything flows ? *Journal of Non-Newtonian Fluid Mech*, *81*, 133–178. https://doi.org/10.1016/S0377-0257(98)00094-9

Bergantz, G. W., Schleicher, J. M., & Burgisser, A. (2017). On the kinematics and dynamics of crystal-rich systems. *Journal of Geophysical Research: Solid Earth*, *122*, 6131–6159. https://doi.org/10.1002/2017JB014218

Burgisser, A., & Bergantz, G. W. (2011). A rapid mechanism to remobilize and homogenize highly crystalline magma bodies. *Nature*, *471*(7337), 212–215. https://doi.org/10.1038/nature09799

Caricchi, L., Burlini, L., Ulmer, P., Gerya, T., Vassalli, M., & Papale, P. (2007). Non-Newtonian rheology of crystal-bearing magmas and implications for magma ascent dynamics. *Earth and Planetary Science Letters*, *264*, 402–419. https://doi.org/10.1016/j.epsl.2007.09.032

Cashman, K. V., Sparks, R. S. J., & Blundy, J. D. (2017). Vertically extensive and unstable magmatic systems: A unified view of igneous processes. *Science*, *355*(6331), eaag3055. https://doi.org/10.1126/science.aag3055

Castruccio, A., Rust, A. C., & Sparks, R. S. (2013). Evolution of crust- and core-dominated lava flows using scaling analysis. *Bulletin of Volcanology*, *75*(1), 1–15. https://doi.org/10.1007/s00445-012-0681-2

Christopher, T. E., Blundy, J., Cashman, K. V., Cole, P., Edmonds, M., Smith, P. J., et al. (2015). Crustal-scale degassing due to magma system destabilization and magma-gas decoupling at Soufrière Hills Volcano, Montserrat. *Geochemistry, Geophysics, Geosystems*, *16*, 2797–2811. https://doi.org/10.1002/2015GC005791

Connolly, J., & Podladchikov, Y. (2013). A hydromechanical model for lower crustal fluid flow, *Metasomatism and the chemical transformation of rock* pp. 599–658). Heidelberg: Springer. https://doi.org/10.1007/978-3-642-28394-9

Costa, A., Caricchi, L., & Bagdassarov, N. (2009). A model for the rheology of particle-bearing suspensions and partially molten rocks. *Geochemistry, Geophysics, Geosystems*, *10*, Q03010. https://doi.org/10.1029/2008GC002138

Couch, S., Sparks, R. S. J., & Carroll, M. R. (2001). Mineral disequilibrium in lavas explained by convective self-mixing in open magma chambers. *Nature*, *411*, 1037–1039.

de Bremond d'Ars, J., Jaupart, C., & Sparks, R. S. J. (1995). Distribution of volcanoes in active margins. *Journal of Geophysical Research*, *100*(B10), 20,421–20,432. https://doi.org/10.1029/95JB02153

Degruyter, W., & Huber, C. (2014). A model for eruption frequency of upper crustal silicic magma chambers. *Earth and Planetary Science Letters*, *403*, 117–130. https://doi.org/10.1016/j.epsl.2014.06.047

Dufek, J., & Bachmann, O. (2010). Quantum magmatism: Magmatic compositional gaps generated by melt-crystal dynamics. *Geology*, *38*(8), 687–690. https://doi.org/10.1130/G30831.1

Hoover, S., Cashman, K. V., & Manga, M. (2001). The yield strength of subliquidus basalts—Experimental results. *Journal of Volcanology and Geothermal Research*, *107*, 1–18.

Huber, C., Bachmann, O., & Dufek, J. (2010). The limitations of melting on the reactivation of silicic mushes. *Journal of Volcanology and Geothermal Research*, *195*(2-4), 97–105. https://doi.org/10.1016/j.jvolgeores.2010.06.006

Huppert, H. E., Sparks, R. S. J., & Turner, J. S. (1982). Effects of volatiles on mixing in calc-alkaline magma systems. *Nature*, *297*(5867), 554–557. https://doi.org/10.1038/297554a0

Huppert, H. E., Sparks, R. S. J., & Turner, J. S. (1984). Some effects of viscosity on the dynamics of replenished magma chambers. *Journal of Geophysical Research*, *89*(B8), 6857–6877.

Jackson, M. D., Cheadle, M. J., & Atherton, M. P. (2003). Quantitative modeling of granitic melt generation and segregation in the continental crust. *Journal of Geophysical Research*, *108*(B7), 2332. https://doi.org/10.1029/2001JB001050

Jaxybulatov, K., Shapiro, N. M., Koulakov, I., Mordret, A., Landès, M., & Sens-Schönfelder, C. (2014). A large magmatic sill complex beneath the Toba caldera. *Science*, *346*(6209), 617–619. https://doi.org/10.1126/science.1258582

Karakas, O., Degruyter, W., Bachmann, O., & Dufek, J. (2017). Lifetime and size of shallow magma bodies controlled by crustal-scale magmatism. *Nature Geoscience*, *10*, 446–450. https://doi.org/10.1038/ngeo2959

Kerr, R. C., & Lister, J. R. (1991). The effects of shape on crystal settling and on the rheology of magmas. *The Journal of Geology*, *99*(3), 457–467.

Lees, J. M. (1992). The magma system of Mount St. Helens: Non-linear high resolution P-wave tomography. *Journal of Volcanology and Geothermal Research*, *53*(1-4), 103–116.

Lejeune, A.-M., & Richet, P. (1995). Rheology of crystal-bearing silicate melts: An experimental study at high viscosities. *Journal of Geophysical Research*, *100*(B3), 4215–4229. https://doi.org/10.1029/94JB02985

Murase, T., & McBirney, A. R. (1973). Properties of some common igneous rocks and their melt at high temperatures. *Geological Society of America Bulletin*, *84*(11), 3563–3592.

Oppenheimer, J., Rust, A. C., Cashman, K. V., & Sandnes, B. (2015). Gas migration regimes and outgassing in particle-rich suspensions. *Frontiers in Physics*, *3*, 1–13. https://doi.org/10.3389/fphy.2015.00060

Parmigiani, A., Huber, C., & Bachmann, O. (2014). Mush microphysics and the reactivation of crystal-rich magma reservoirs. *Journal of Geophysical Research: Solid Earth*, *119*, 6308–6322. https://doi.org/10.1002/2014JB011124

Putirka, K. D. (2017). Down the crater: Where magmas are stored and why they erupt. *Elements*, *13*(1), 11–16. https://doi.org/10.2113/gselements.13.1.11

Pyle, D. M. (2015). Sizes of volcanic eruptions. In *The encyclopedia of volcanoes* (2nd ed., pp. 257–264). Amsterdam: Elsevier Inc. https://doi.org/10.1016/B978-0-12-385938-9.00013-4

Romine, W. L., Whittington, A. G., Nabelek, P. I., & Hofmeister, A. M. (2012). Thermal diffusivity of rhyolitic glasses and melts: Effects of temperature, crystals and dissolved water. *Bulletin of Volcanology*, *74*(10), 2273–2287. https://doi.org/10.1007/s00445-012-0661-6

Rougier, J., Sparks, R. S. J., Cashman, K. V., & Brown, S. K. (2018). The global magnitude-frequency relationship for large explosive volcanic eruptions. *Earth and Planetary Science Letters*, *482*, 621–629. https://doi.org/10.1016/j.epsl.2017.11.015

Saar, M. O., Manga, M., Cashman, K. V., & Fremouw, S. (2001). Numerical models of the onset of yield strength in crystal-melt suspensions. *Earth and Planetary Science Letters*, *187*(3-4), 367–379. https://doi.org/10.1016/S0012-821X(01)00289-8

Sandnes, B., Flekkøy, E. G., Knudsen, H. A., Måløy, K. J., & See, H. (2011). Patterns and flow in frictional fluid dynamics. *Nature Communications*, *2*(288). https://doi.org/10.1038/ncomms1289

Scaillet, B., Holtz, F., & Pichavant, M. (1998). Phase equilibrium constraints on the viscosity of silicic magmas 1. Volcanic-plutonic comparison. *Journal of Geophysical Research*, *103*(B11), 27,257–27,266. https://doi.org/10.1029/98JB02469

Schmeling, H., Marquart, G., & Grebe, M. (2017). A porous flow approach to model thermal non-equilibrium applicable to melt migration. *Geophysical Journal International*, *212*, 119–138. https://doi.org/10.1093/gji/ggx406/4411804

Scott, D. R., & Stevenson, D. J. (1984). Magma solitons. *Geophysical Research Letters*, *11*(11), 1161–1164.

Scott, D. R., & Stevenson, D. J. (1986). Magma ascent by porous flow. *Journal of Geophysical Research*, *91*(B9), 9283–9296.

Sheldrake, T. E., Sparks, R. S., Cashman, K. V., Wadge, G., & Aspinall, W. P. (2016). Similarities and differences in the historical records of lava dome-building volcanoes: Implications for understanding magmatic processes and eruption forecasting. *Earth-Science Reviews*, *160*, 240–263. https://doi.org/10.1016/j.earscirev.2016.07.013

Solano, J. M. S., Jackson, M. D., Sparks, R. S. J., Blundy, J. D., & Annen, C. J. (2012). Melt segregation in deep crustal hot zones: A mechanism for chemical differentiation, crustal assimilation and the formation of evolved magmas. *Journal of Petrology*, *53*(10), 1999–2026. https://doi.org/10.1093/petrology/egs041

Sparks, R. S. J., & Cashman, K. V. (2017). Dynamic magma systems: Implications for forecasting volcanic activity. *Elements*, *13*(1), 35–40. https://doi.org/10.2113/gselements.13.1.35

Sweeney, H., Kerswell, R. R., & Mullin, T. (2013). Rayleigh-Taylor instability in a finite cylinder: Linear stability analysis and long-time fingering solutions. *Journal of Fluid Mechanics*, *734*(2013), 338–362. https://doi.org/10.1017/jfm.2013.492

Tarasewicz, J., White, R. S., Woods, A. W., Brandsdóttir, B., & Gudmundsson, M. T. (2012). Magma mobilization by downward-propagating decompression of the Eyjafjallajökull volcanic plumbing system. *Geophysical Research Letters*, *39*, L19309. https://doi.org/10.1029/2012GL053518

Turcotte, D., & Schubert, G. (1982). *Geodynamics: Applications of continuum physics to geological problems*. New-York: Wiley.

Waddell, J. T., Niederhaus, C. E., & Jacobs, J. W. (2001). Experimental study of Rayleigh-Taylor instability: Low Atwood number liquid systems with single-mode initial perturbations. *Physics of Fluids*, *13*(5), 1263–1273. https://doi.org/10.1063/1.1359762

White, S. M., Crisp, J. A., & Spera, F. J. (2006). Long-term volumetric eruption rates and magma budgets. *Geochemistry, Geophysics, Geosystems*, *7*, Q03010. https://doi.org/10.1029/2005GC001002

Whitehead, J. A., & Luther, D. (1975). Dynamics of laboratory diapir and plume models. *Journal of Geophysical Research*, *80*(5), 705–717. https://doi.org/10.1029/JB080i005p00705

Whitney, J. A., & Stormer, J. C. (1985). Mineralogy, petrology, and magmatic conditions from the Fish Canyon Tuff, Central San Juan Volcanic Field, Colorado. *Journal of Petrology*, *26*(3), 726–762. https://doi.org/10.1093/petrology/26. 3.726

Whittington, A. G., Hofmeister, A. M., & Nabelek, P. I. (2009). Temperature-dependent thermal diffusivity of the Earth's crust and implications for magmatism. *Nature*, *458*(7236), 319–321. https://doi.org/10.1038/nature07818

Wilkinson, J. P., & Jacobs, J. W. (2007). Experimental study of the single-mode three-dimensional Rayleigh-Taylor instability. *Physics of Fluids*, *19*(12), 124102. https://doi.org/10.1063/1.2813548